Shaping the emission directivity of single quantum dots in dielectric nanodisks exploiting Mie resonances

Cristina Cruciano,[†] Davide Rocco,[‡] Armando Genco,[*,†] Andrea Tognazzi,[¶] Andrea Locatelli,[‡] Luca Carletti,[‡] Alexey Fedorov,[§] Charalambos Louca,[†,‖] Giulio Tavani,[†] Luca Lovisolo,[⊥] Artur Tuktamyshev,[#] Lucio Andreani,[@] Matteo Galli,[@] Giulio Cerullo,[†] Giuseppe Leo,[⊥] Stefano Sanguinetti,[#] Costantino De Angelis,[‡] and Monica Bollani[§]

†*Department of Physics, Politecnico of Milano, Piazza Leonardo Da Vinci 32, 20133 Milano, Italy*

‡*Department of Information Engineering, University of Brescia, via Branze 38, 25123, Brescia, Italy*

¶*Department of Engineering, University of Palermo, viale delle scienze 10, 90128, Palermo, Italy*

§*Institute of photonics and of nanotechnologies- National Researcher Council (IFN-CNR), LNESS laboratory, Piazza Leonardo Da Vinci 32, 20133 Milano, Italy*

‖*NanoPhotonics Centre, Cavendish Laboratory, Department of Physics, JJ Thompson Ave, Cambridge, UK*

⊥*Matériaux et Phénomènes Quantiques, Université Paris Cité and CNRS, 10 rue A. Domon et L. Duquet, Paris, 75013 France*

#*Department of Material Science, University of Milano Bicocca via Cozzi 55, 20126 Milano, Italy*

@*Department of Physics, University of Pavia, via Bassi 6, I-27100 Pavia, Italy*

E-mail: armando.genco@polimi.it

Abstract

Manipulating the optical landscape of single quantum dots (QDs) is essential to increase the emitted photons output, enhancing their performance as chemical sensors and single photon sources. Micro-optical structures are typically used for this task, with the drawback of the large size compared to the embedded single emitters. Nanophotonic architectures hold the promise to modify dramatically the emission properties of QDs, boosting light-matter interactions at the nano-scale, in ultracompact devices. Here we investigate the interplay between gallium arsenide (GaAs) single QDs and aluminum gallium arsenide (AlGaAs) nanostructures, capitalizing on the Kerker condition for precise control of the quantum dot emission directivity. An extensive analysis of the photoluminescence spectra of several QDs embedded in nanodisks revealed a pronounced directivity enhancement owing to the Kerker effect, confirmed by theoretical simulations, resulting in a 14-fold increase of emitted intensity. Angle-resolved spectroscopy experiments also proved that the integration of GaAs QDs within nanostructures determines a precise angled emission, offering a distinctive avenue for manipulating the spatial characteristics of emitted light exploiting Mie resonances. This work contributes to understanding of quantum dot integration in nanostructures and suggests potential improvements for applications in optical communications.

Introduction

The convergence of quantum optics and nanophotonics has sparkled countless innovations and discoveries, propelling the field towards unprecedented precision in the control of light-matter interactions at the nanoscale. Quantum dots (QDs), as versatile single photon emitters, have become a fundamental building block for photonic quantum information, communications, and sensing technologies.[1] Yet, to fully exploit their quantum nature, researchers are increasingly focused on overcoming inherent challenges, such as the effective control and manipulation of QDs emission. To this aim, it is of key importance to engineer the pho-

tonic landscape around the QD on a nano- or micro-scale, channeling the emitted photons into highly directional optical modes, and out-coupling them for external use in quantum computation and communications.[2] Several micro-optical architectures have been proposed to maximize the overall photon extraction efficiency, keeping a high degree of single photon indistinguishability (up to 99%).[3] Gate-tunable open microcavities,[4] micropillars[5–7] and photonic crystal waveguides[8–11] are among the best structures used for optimized QD-based single photon sources, reaching end-to-end photon generation efficiencies exceeding 50%.[4] Photonic nanostructures further expand the possibilities to shape the light-emitter interactions acting on the local electromagnetic environment of the QD at the nano-scale, with the additional advantage of shrinking the size of the device to the sub-micron scale, useful for on-chip integration.

In this context, the Kerker condition has risen to prominence as a pivotal tool for manipulating the electromagnetic landscape within nanostructures[12,13] and at microwave frequencies.[14] Originally conceived for the control of classical light scattering, the Kerker condition has been recently predicted to be extremely useful also in the quantum domain.[15] This innovative paradigm introduces a powerful strategy to direct the emission properties of quantum dots by strategically integrating them with optical nanostructures. The Kerker effect, characterized by a significant asymmetry in forward-to-backward electromagnetic scattering, is a fundamental and versatile physical mechanism for directing the scattering of an electromagnetic plane wave using Mie resonant particles. This unidirectional scattering mechanism is based on the interference of electromagnetic multipolar moments induced in the Mie scatterers.[13] Thus, by optimizing the excited multipoles in the nanostructure it is possible to obtain the zero-back scattering or zero-forward scattering conditions. While the condition has been extended to higher order multipoles, the case of most immediate practical realization is the one which involves the electric dipole (ED) and magnetic dipole (MD) resonances.[16–18] When these two multipoles have the same amplitude and zero phase difference, then we can obtain a Kerker-type emission in the forward direction (first Kerker condition), whereas if the phase

difference is π ~~rad~~, the radiation is in the backward direction (second Kerker condition).[19] A moderately high forward-to-backward scattering ratio can be achieved under the first Kerker condition.

All-dielectric nanostructures showed a wide range of applications concerning the optimization of their radiation emission both in isolated and metasurface configuration.[20–26] By manipulating the scattering properties of dielectric nanoparticles, researchers theoretically proposed to sculpt the emission characteristics of QDs with unprecedented precision.[19] However, there are only few experimental results showing the interaction of quantum sources with dielectric nanoantennas.[27–30]

Here, we test both theoretically and experimentally the behavior of few GaAs-based QDs working as quantum emitters embedded within AlGaAs dielectric nanoresonators and exploit the Kerker condition to modify the emission directivity based on the position of the QDs within the nanodisks. By employing a novel fabrication method, we create AlGaAs nanodisks on a AlO_x transparent layer with a low number of QDs (about 8 -12 dots for cylinder) located at two different heights within the pillar, which correspond to forward and backward scattering Kerker conditions. Angle-resolved photoluminescence ~~spectroscopy~~ (PL) reveals a strong dependence of the angular emission pattern on the position of the QDs within the base area of the pillar. Performing a statistical analysis on more than 150 QDs, we observe a dramatic enhancement of the PL intensity by more than one order of magnitude when the emitters reside close to the top of the nanodisks, demonstrating the efficacy of the Kerker effect. The integration of QDs with nanostructures leveraging the Kerker condition not only advances our fundamental understanding of light-matter interactions, but also opens pathways to practical applications, from quantum information processing to advanced sensing technologies.

Results and discussion

Numerical Simulation

In order to emulate the scattering behavior of the proposed active photonic system, we perform finite-element simulations in Comsol Multiphysics. In the numerical study we consider an AlGaAs cylinder with radius ~~of~~ 110 nm and height 175 nm on a low refractive index (n=1.6) substrate. For the dispersion of AlGaAs we consider the permittivity values as in.[31] The QD source is modeled as a point-like x-polarized electric dipole positioned at the center of the cylinder at different heights (see insets of Fig. 1a). From our simulations, we choose two different vertical positions for the QDs to better satisfy the Kerker condition in the fabricated nanodisks, named series TOP and series BOTTOM. In order to find such values, we performed a parametric study as a function of both the QD vertical position and the emission wavelength. The obtained wavelength and position dependent scattering cross section is shown in Fig. 1b. The graph highlights three zones of maximum emission that correspond to the excitation of the ED and MD resonance modes in the AlGaAs cylinder. The dashed black lines indicate the QD position at which the amplitudes of ED and MD are the same at the wavelength of 760 nm, that correspond to the fabricated series TOP and BOTTOM. It should be noted that the excitation of these resonances is not perfectly symmetrical with respect to the variation in the height position of the QD due to the presence of the substrate underneath the cylinder. The ideal Kerker condition is achieved when the ED and MD have the same amplitude and zero or π rad phase difference to reach the unidirectional emission towards the air or substrate region, respectively. As reported in,[19] the performance in terms of emission directivity can be expressed by a front-to-back (F/B) ratio, defined as the ratio between the magnitude of the electric far field at $\theta = 0$ rad and at $\theta = \pi$ rad, where θ is defined as in the reference system of Fig. 1. In particular, Fig. 1c shows that when the QD is positioned at a height of about 120 nm (series TOP) from the base of the cylinder the F/B ratio is maximum, while it is minimum when the position of the QD is 40 nm (se-

ries BOTTOM) around the wavelength of 760 nm. These preliminary simulations confirm how it is possible, depending on the QD vertical position, to engineer the emission from the nanostructure by almost fulfilling the first Kerker condition. In particular, for positions of the QD around 120 nm in height, the light radiation is redirected mainly towards the air region (i.e. ED≈MD), while for heights of around 40 nm the emission is mainly directed towards the substrate (i.e. ED≈−MD). Furthermore, in the simulations, we also considered the more realistic case of finite thickness (equal to 1 μm) for the AlOx substrate with an underlying GaAs layer. For the latter case, the emission properties do not undergo notable variations with respect to the case of single AlOx layer, therefore we considered in the subsequent numerical analysis, the less time-consuming computational case of semi-infinite AlOx substrate only.

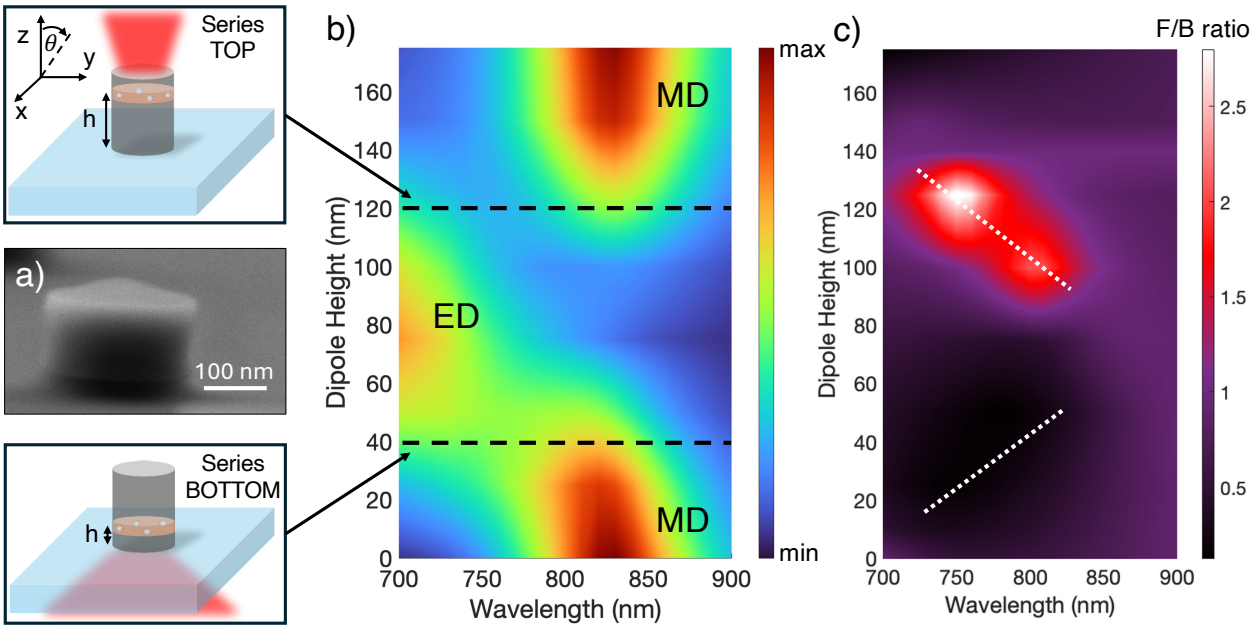

Figure 1: a) Scanning electron microscope (SEM) image of fabricated nanodisk after all fabrication processes. Due to the low density and nanometric size of QDs, it is not possible to visualize their presence in high-resolution SEM image. b) Normalized scattering cross section as a function of the wavelength and dipole height. The black dashed lines indicates the two considered QDs positions as schematically illustrated by the two insets with the sketch of the QD-loaded nanodisks of the series TOP and BOTTOM. c) Ratio between the far field radiated towards air and substrate (F/B ratio) as a function of the wavelength and dipole height. The white dotted lines highlight the high directivity regions.

In addition, we analyze how the position of the QD within the base area of the nanodisk influences the radiation in terms of scattered power and emission directivity. For the two reference heights (120 nm and 40 nm for the series TOP and BOTTOM, respectively) we evaluated the emission variation of the scattered light from our platform as a function of the offset of the QD, along the x or y axis, with respect to the axis of the nanoresonator. The results of this study are depicted in the polar plots of Fig.2, where the gray shaded areas represent the angular range outside the numerical aperture (NA) of the objective used in the experiments, equal to 0.5. In particular, for the TOP series, when the QD is moved along the x-axis from the center (Fig.2a), a slightly angled radiation pattern is observed, with a maximum emission that goes from the vertical direction (θ=0 rad) up to approximately θ=$\pi/4$ rad when the QD is close to the border of the cylinder. Instead, moving the QD along the y direction degrades the unidirectional emission, and for $d \geq 70$ nm the emission side-lobes become predominant (Fig.2b). This behavior is due to the excitation of higher order modes in the cylinder. For the QD in the series BOTTOM, minor lobes are emitted into the air region since the main emission is radiated toward the substrate (Fig.2c,2d).[19]

Fabrication

The investigated nanostructures are fabricated by a combination of molecular beam epitaxy (MBE), electron beam lithography (EBL), inductively coupled plasma - reactive ion etching (ICP-RIE) and local oxidation thermal processes.

The samples are grown in a conventional MBE system on GaAs(001) substrates. The growths are performed using a valved cell for the optimal control of the As_4 flow and monitored by *in situ* ~~by~~ reflection high-energy electron diffraction (RHEED). After the oxide desorption in As atmosphere at 580 °C, an atomically smooth surface is prepared by growing ∼250 nm thick GaAs buffer layer with a rate of 0.5 ~~ML~~/s. Then, 1 μm thick AlAs film is deposited at T=620°C with a rate 0.5 ML/s. This structure stack is identical for the two

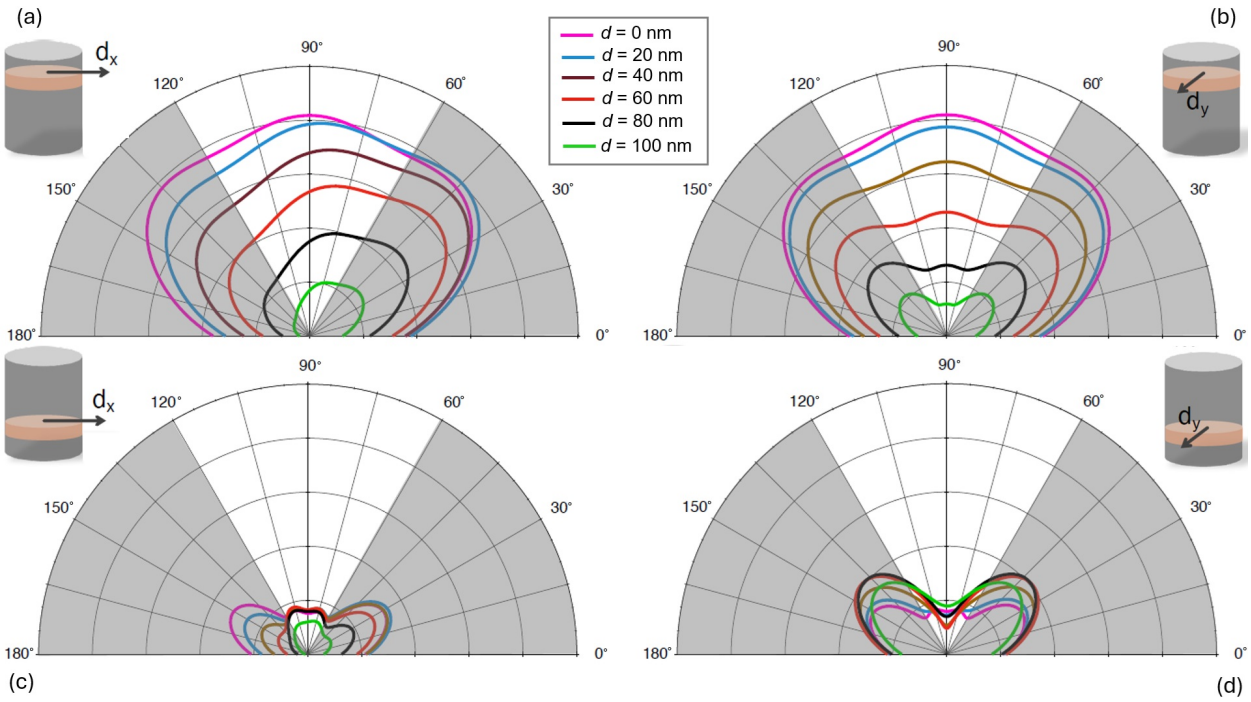

Figure 2: Calculated radiation pattern in the air region as a function of the QD displacement along the x (left panels) or y axis (right panels) for the two reference heights of the series TOP ((a) and (b)) and BOTTOM ((c) and (d)) highlighted by the insets. The gray area indicates the region outside the NA used in the experiment.

growth series (indicated as TOP and BOTTOM) and, following a selective external oxidation process, it is used for optical insulation. At the same temperature, an AlGaAs layer with 18% Al content of 40 nm (series BOTTOM) or 115 nm (series TOP) is deposited. On top of AlGaAs structure, a layer of self-assembly QD is performed using the Droplet Epitaxy (DE) technique,[32] which permits the fabrication of strain free[33] and strained[34] III-V QDs with high control of size[35] and symmetry.[36] The Droplet Epitaxy is a two step growth step process, which consists in: 1) the formation of tiny droplets of group III metal by irradiation of the metal on the substrate surface in absence of As; 2) the annealing of the droplets in an As atmosphere to convert them in three-dimensional nanoislands.[37] For the DE step the substrate temperature is decreased to 170°C and the As valve is closed at 420°C in order to deplete the growth chamber of the arsenic molecules. The RHEED pattern clearly shows a c(4x4) surface reconstruction. Ga adatoms are deposited on the AlGaAs surface at a temperature of 170°C with a flow of 0.1 ML/s. By this condition we expect to have a QD density of about 400 droplets per square micron. The first monolayer of Ga, interacting with the As-rich c(4x4) reconstructed surface, establishes a Ga-stabilized (3x6) reconstruction. The droplets are subsequently formed by the remaining Ga atoms. In total, 2.5 MLs of Ga are deposited and self-assembled in droplets. Then the Ga droplets are exposed to an As beam equivalent pressure of 5×10^{-5} Torr at 170°C for 3 min to crystallize them into GaAs nanoislands.[37] Subsequently, the nanocrystals undergoes a flash procedure, consisting of 10 min at 380°C in an As pressure of 4×10^{-6} Torr. The GaAs dots are then covered by 30 ML of AlGaAs ($\sim$ 8 nm) by migration enhanced epitaxy.[38] Finally, the temperature is increased up to 620°C and AlGaAs alloys with 18% Al are deposited on top of the QDs layer to reach a total thickness of 175 nm. Both structures (TOP and BOTTOM series) are capped with $\sim$ 5 nm of GaAs to prevent the oxidation process. A schematic of the sample structures is shown in Fig. 3a. The EBL is carried out in order to define circular structures with radius varying from 80 nm to 140 nm. A double layer of polymethyl methacrylate (PMMA) diluted in chlorobenzene, respectively, at 3.5% and 1.5% is employed. The dose used for

the structures is 350 μC/cm^2 for larger diameters, increased to 390 μ/cm^2 for smaller ones. After exposure, PMMA is developed for 90 s in a diluted solution of methyl isobutyl ketone and isopropanol in a 1:3 ratio to obtain well-defined profiles.[39] The pattern is transferred down to the bottom AlAs by non-selective ICP-RIE with $SiCl_4$:Ar chemical treatment. The etching depth of 175 nm for both series is controlled by laser interferometry, defining the AlGaAs nanocylinders. The AlAs layer is then thermally oxidized into AlO_x, resulting in an optical confinement in the active layer because of the refractive index difference between $Al_{0.18}Ga_{0.82}As$ (n≈3.3) and AlO_x (n≈1.6).[40] The selective oxidation of the Al-rich layers is performed in water vapor at a temperature of 300°C, which leads to the formation of the aluminum oxide.[41] Using nanolithographic tuning, cylinders with radii just a few nanometers apart are realized, covering surfaces of over 100 square microns and periods of 3 microns (Fig. 3b). The optimization of the dry etching process is well visible in the high-resolution SEM image of a single cylinder, where lateral etching imperfections are negligible (Fig. 3c).

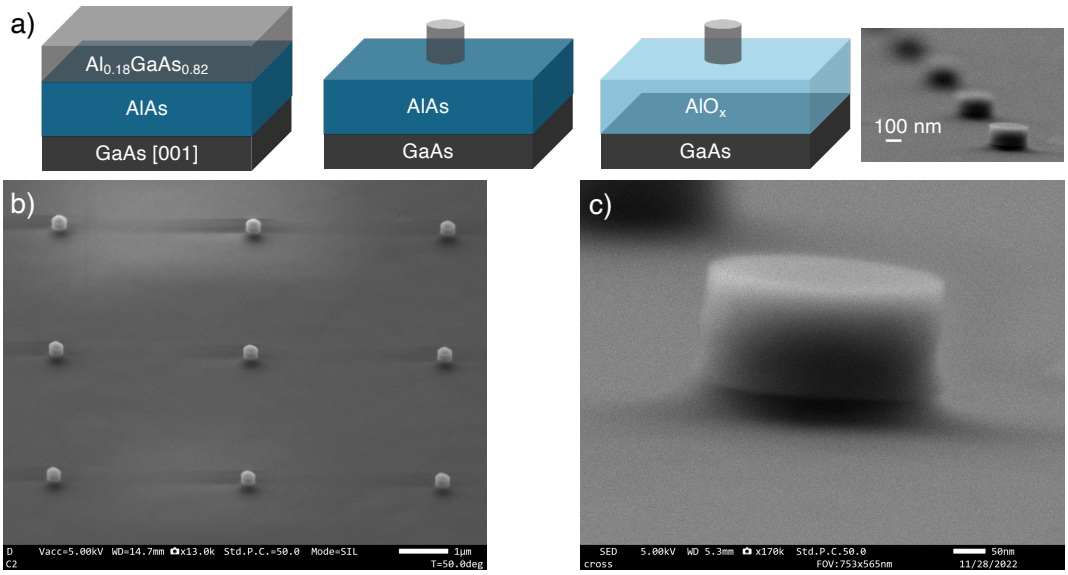

Figure 3: a) Representation of the fabrication steps starting form the MBE growth, EBL and RIE processes and finally selective oxidation treatment. b) SEM tilted view image of patterned cylinders, whose radius changes every line thanks to the optimized lithographic tuning. c) High resolution SEM of a single AlGaAs cylinder, inside which are placed a few GaAs QDs, positioned above the oxidized AlOx layer.

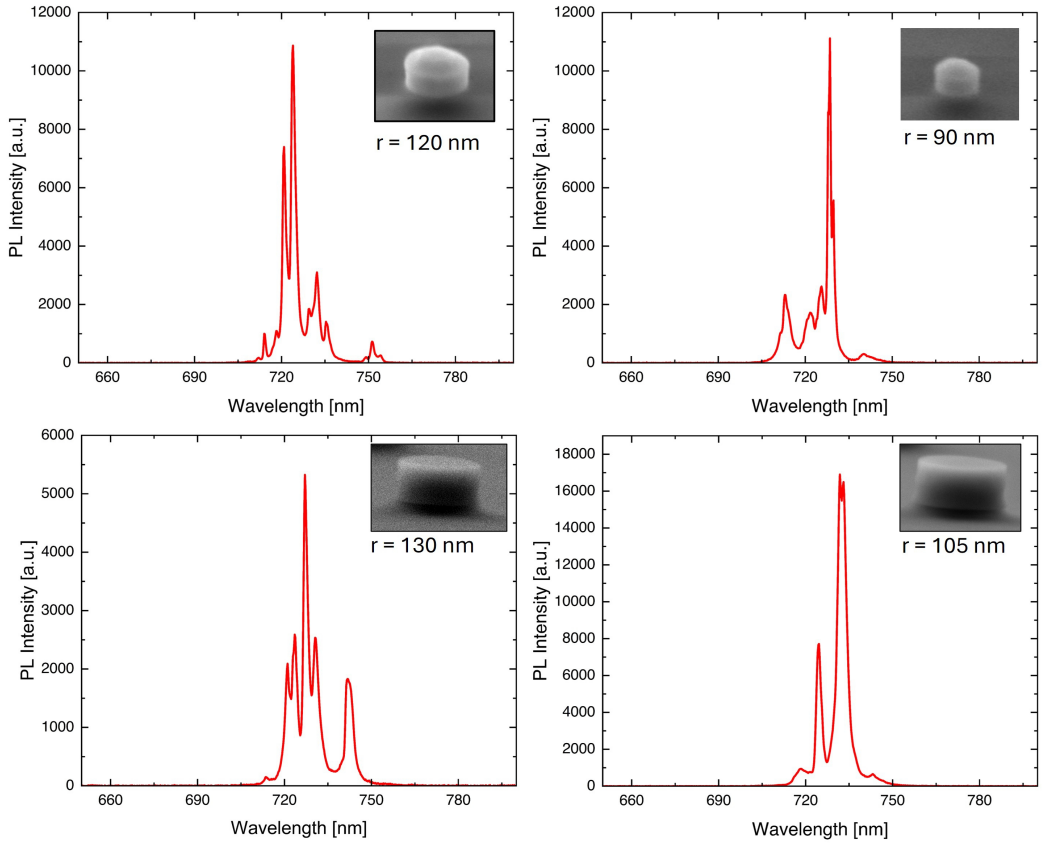

Figure 4: PL spectra collected from the single nanodisk for different patterned areas for the TOP series. Nanocylinders with different radii are analyzed, showing PL signals of different intensity and peak position, mainly due to the slightly different dimension of QDs present in the cylinder and their position with respect of the cylinder ~~center~~.

Spectroscopy experiments

To investigate the directivity and the angular emission pattern of the QDs embedded in the nanodisks, we employed a custom-made microscopy setup, equipped with a 50x objective lens (NA: 0.5) and a 630 nm CW laser to perform PL spectroscopy at 8K in a closed-loop He cryostat, both in real space and in Fourier space (see more details in the Supplementary Information). Four PL spectra measured in real space, exemplary for the QDs emission in a series of cylinders with different radii, are reported in Figure 4. Each PL spectrum shows few peaks due to the emission of single QDs. The different emission energy depends on the slightly different size of the QDs [32] and their position relative to the center of the cylinder. The QD embedded ~~closed~~ to the walls ~~has~~ low PL intensity compared to QDs positioned in the center due to the non-radiative recombination process. We use ~~Fourier~~ spectroscopy since it allows to easily characterize both the spectrum and the angular pattern of the light emitted/transmitted/reflected from optical micro- and nano-structures and metasurfaces in a broad angular range, limited by the NA of the objective.[42] In our setup, the PL emitted from the sample is collected by the excitation objective and sent to a spectrometer equipped with a CCD camera. By adding a Fourier lens in the detection path of the microscope, we image the back focal plane of the objective lens, defined as the plane normal to the lens~~es~~ optical axis situated at a focal distance behind the objective. On this plane, every point corresponds to a specific value of the incoming light wavevector k, proportional to the angle of light rays measured from the lens axis. Given the NA of our objective, the detected angular field of view (FOV) spans from 0° to 30°. By closing the slit of the spectrometer, we select just a vertical slice of the Fourier-plane image which is then diffracted by the grating of the spectrometer (Figure S1). This results in a map of PL intensity as a function of θ_y and wavelength, recorded by the camera.

Figures 5 (a,b) show the PL maps as a function of angle and wavelength recorded for two nanodisks, one for the series TOP (a) and one for the series BOTTOM (b). It can be noticed that the intensity of the QDs emission varies as a function of the angle. This trend

is better represented in Figures 5 (c,d), which show horizontal cross-sections of the maps in Fig. 5 (a,b) taken at the peak wavelength of the main emission lines. The abrupt changes in intensity visible in the curves are attributed to small defects in the optical elements used in the setup. It can be seen that, even inside the same nanodisk, the emission follows different angular ~~behaviour~~ for different QDs, increasing or decreasing in intensity with the angle. Figures 5 (e,f) show vertical cross-sections of the maps in Fig. 5 (a,b) taken at 0° and 25° where the difference in intensity between the QD emission lines can be appreciated more clearly. On the other hand, the QD spectral shape shows negligible variations changing the angle. Comparing these results with the simulations in Fig. 2, we argue that an increase of emission at higher angles can be related to QDs positioned closer to the edge of the nanodisks, e.g. the QD emitting at 732 nm in Figs. 5(a,c,e). Therefore, angle resolved PL emission spectroscopy can help to discern the position of single QDs within the base area of each nanodisk, which cannot be controlled at the fabrication level and is very difficult to ~~understand~~ without using more complex and often invasive techniques.

We performed a statistical analysis of the collected PL spectra in real and Fourier space on several nanocylinders with different radius and with QDs positioned at the top and at the bottom. Figure 6 (a) shows the distribution of the PL peak intensities as a function of the peak wavelength for more than 150 QD emission lines extracted from the PL real-space measurements on nanodisks of series TOP and series BOTTOM (red and blue dots in Fig. 6a respectively) with different radii. Although the intensity distribution is quite broad for both the series, the QDs in series TOP are clearly brighter than the ones in series BOTTOM. In fact, the calculated average intensity of all the QDs in the former series is about one order of magnitude higher than in the latter (dashed lines in Fig. 6a).

We compare these results with the simulated scattered power for the series TOP and BOTTOM, as a function of the ~~position~~ of the QD from the central axis of the pillar (Figure 6(b)). Interestingly, even by moving the QD from the center of the nanodisk up to 40 nm (both along the x or y direction), the scattered power of series TOP is always more

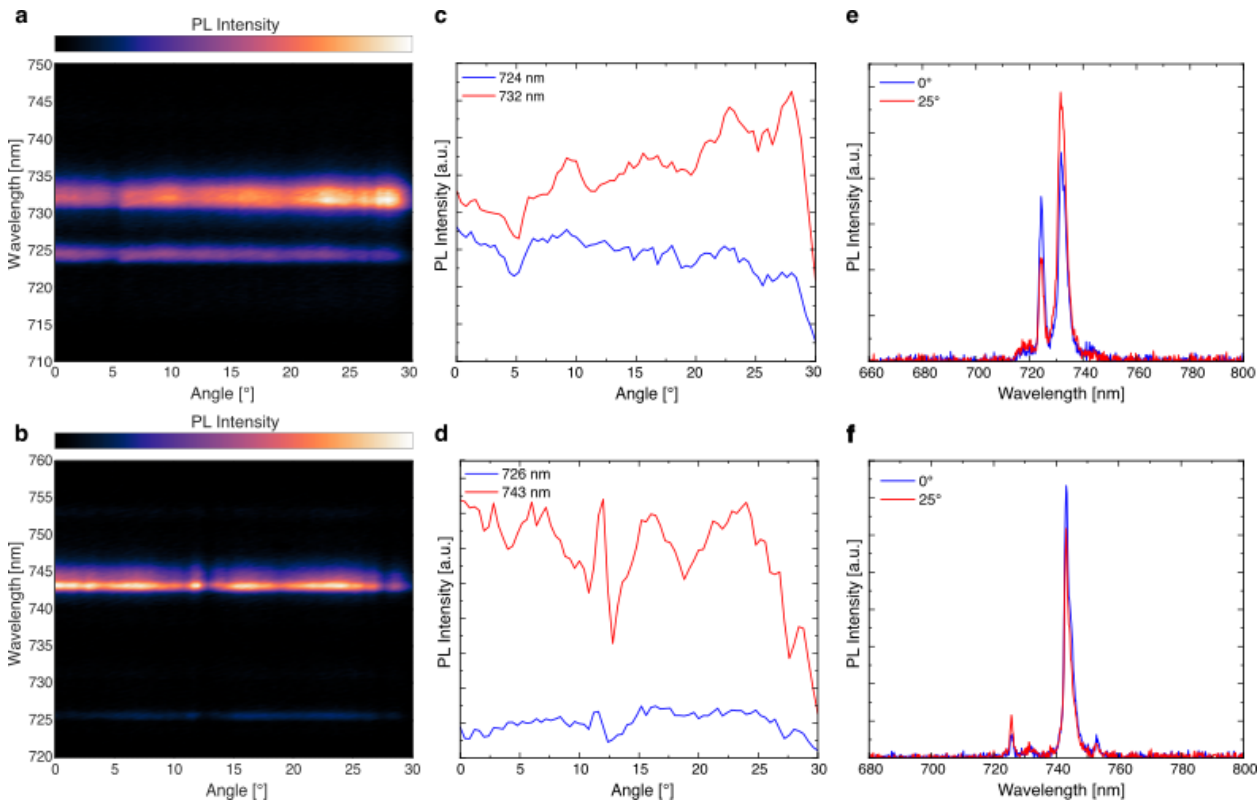

Figure 5: (a,b) PL Fourier space maps showing the emission lines of nanodisks with QDs in series TOP (a) and BOTTOM (b). (c,d) Horizontal cross sections of (a) and (b) taken at PL peak wavelengths of the QDs showing the angular emission pattern. (e,f) Vertical cross sections of (a) and (b) showing the PL spectra at different angles, at 0° (e) and 25° (f).

than an order of magnitude higher compared to series BOTTOM, as a consequence of the Kerker effect. This further demonstrates that the QDs positioned around the center of the nanodisk have a good coupling with the ED and MD resonances and consequently guarantee a Kerker-like emission.

For every measured QD angular emission pattern, taken from the horizontal cross-section of the PL Fourier maps at the QDs peak wavelength, e.g. Figs. 5 (c,d), we calculated the weighted averaged angle (or angular barycentre), defined as the product between the PL intensity at each angle and the emission angle, divided by the total PL intensity emitted over the spanned angular range. In the sample with the QDs on top (red histogram in Fig. 6c), the distribution shows a maximum between 14° and 15°, at roughly half of the total angular FOV (30°). On the other hand, for the sample with the QDs at the bottom (blue histogram in Fig. 6c) the distribution peak is shifted closer to the normal direction, between 12° and 13°, suggesting a QD emission directionality more pronounced towards small angles in the latter configuration. This behaviour is due to the non-symmetric QDs distribution inside the nanocylinder. The QDs are placed randomly across the base area of the nanodisks and, according to our simulations in Fig.2, the maximum of the emission inside the NA ~~can be~~ close to zero angle in series BOTTOM even for large displacements along the x axis. Therefore, for off centered QDs the emission ~~can be~~ distributed over smaller angles for series BOTTOM compared to series TOP (see for instance the green and black curves of Fig. 2), still resulting in a much higher overall scattered power in the latter sample.

Figure 6(d) plots the average PL intensity of the two series as a function of the nanodisk radius. Regardless of the radius dimension, the PL peaks intensity in the series TOP is always much higher than when the QDs are located at the bottom. The maximum power ratio (PR), defined as the averaged PL intensity of series TOP divided by the one of series BOTTOM, is about 14 for radii between 95 nm and 105 nm, where the Kerker condition is most effective.

To further validate the measurements, we numerically computed the PR as the scattered

power for QD at the top position in a NA equal to 0.5 divided by the scattered power for QD at the bottom ~~poistion~~ in the same NA as a function of the AlGaAs pillar radius (see inset of Fig. 6d). The maximum theoretical PR is reached for a radius of 110 nm, with a value very close to the experimental one. We underline that this small geometrical mismatch with respect to the nominal value of the AlGaAs pillar radius is completely within the fabrication tolerance inaccuracy for such structures.

Conclusions

In this work, we have shown how the integration of GaAs ~~quantum dots~~ in AlGaAs nanostructures can be used for manipulating the emitted light by exploiting the Mie resonances sustained inside the AlGaAs volume for a strong enhancement of the outcoupled PL. After presenting the theoretical background, we fabricated the optimized structures based on numerical simulations and measure their emission ~~behavior~~. Changing the vertical position of the dots by just 80 nm, we found a dramatic increase of the PL directivity from QDs in forward versus backward scattering Kerker conditions. Moreover, we have shown how small variations of the QD position within the nanodisk can substantially modify the angular emission pattern. The experimental results align very well with the theoretical computations. Our results may open new routes for the light emission control in single emitters with possible applications in integrated optics, communication, and sensing. The interaction between QDs and optical nanostructures, guided by the principles of the Kerker condition, has the potential to boost QDs emission in the dynamic interplay between light and matter on the nanoscale.

Acknowledgement

The authors acknowledge financial support by the European Union – Next Generation EU PRIN 2022 project GRACE6G (2022H7RR4F), PRIN 2022 PNRR project FLAIRS

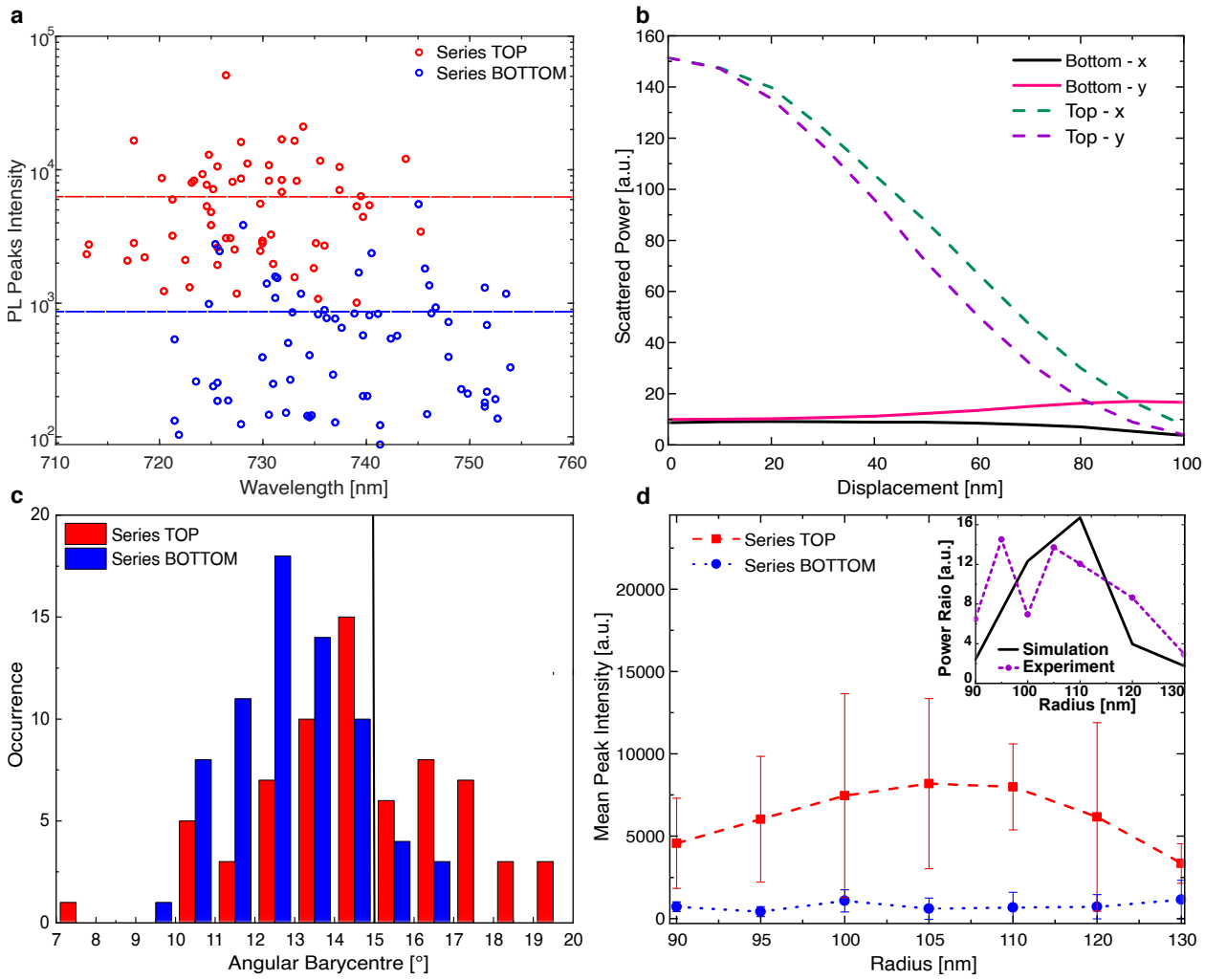

Figure 6: (a) QD PL peak as a function of the wavelength extracted from the real space PL measurements for both the series (red dots: series TOP, blue dots: series BOTTOM). The dashed lines refer to the averaged PL intensity for the two series. (b) Simulations of the scattered power of the QDs as a function of the displacement from the center of the nanodisk for the series with QDs on top (dashed lines) and at the bottom (solid lines) (c) Histograms of the angular barycenter calculated for every QD emission pattern taken from the Fourier space measurements. The black vertical line is at half of the angular FOV. For the series TOP (red columns) the distribution peaks between 14° and 15°, while for series BOTTOM (blue columns) the distribution is shifted between 12° and 13°. (d) Average PL peak intensity of QDs as a function of the nanodisk radius for the series TOP and BOTTOM (red and blue squares). The error bars are the standard deviations extracted from the statistics. Inset: simulated and experimental PR versus the nanodisk radius.

(P2022RFF9K) and PNRR MUR project PE0000023 - NQSTI and project CN00000013 ICSC. A. Tognazzi acknowledges the financial support from the European Union through "FESR o FSE, PON Ricerca e Innovazione 2014-2020 - DM 1062/2021" and the University of Palermo through "Fondo Finalizzato alla Ricerca di Ateneo 2024 (FFR2024)". The authors acknowledge the HORIZON EUROPE European Innovation Council (101130384, HORIZONEIC-2023-PATHFINDEROPEN-01, QUONDENSATE).

References

(1) Yang, L.; Zhang, S.; Xu, B.; Jiang, J.; Cai, B.; Lv, X.; Zou, Y.; Fan, Z.; Yang, H.; Zeng, H. I–III–VI Quantum Dots and Derivatives: Design, Synthesis, and Properties for Light-Emitting Diodes. *Nano Letters* **2023**, *23*, 2443–2453.

(2) Lodahl, P.; Mahmoodian, S.; Stobbe, S. Interfacing single photons and single quantum dots with photonic nanostructures. *Reviews of Modern Physics* **2015**, *87*, 347–400.

(3) Arakawa, Y.; Holmes, M. J. Progress in quantum-dot single photon sources for quantum information technologies: A broad spectrum overview. *Applied Physics Reviews* **2020**, *7*.

(4) Tomm, N.; Javadi, A.; Antoniadis, N. O.; Najer, D.; Löbl, M. C.; Korsch, A. R.; Schott, R.; Valentin, S. R.; Wieck, A. D.; Ludwig, A.; others A bright and fast source of coherent single photons. *Nature Nanotechnology* **2021**, *16*, 399–403.

(5) Somaschi, N.; Giesz, V.; De Santis, L.; Loredo, J.; Almeida, M. P.; Hornecker, G.; Portalupi, S. L.; Grange, T.; Anton, C.; Demory, J.; others Near-optimal single-photon sources in the solid state. *Nature Photonics* **2016**, *10*, 340–345.

(6) Wang, H.; Duan, Z.-C.; Li, Y.-H.; Chen, S.; Li, J.-P.; He, Y.-M.; Chen, M.-C.; He, Y.; Ding, X.; Peng, C.-Z.; others Near-transform-limited single photons from an efficient solid-state quantum emitter. *Physical Review Letters* **2016**, *116*, 213601.

(7) Wang, H.; He, Y.-M.; Chung, T.-H.; Hu, H.; Yu, Y.; Chen, S.; Ding, X.; Chen, M.-C.; Qin, J.; Yang, X.; others Towards optimal single-photon sources from polarized microcavities. *Nature Photonics* **2019**, *13*, 770–775.

(8) Uppu, R.; Pedersen, F. T.; Wang, Y.; Olesen, C. T.; Papon, C.; Zhou, X.; Midolo, L.; Scholz, S.; Wieck, A. D.; Ludwig, A.; others Scalable integrated single-photon source. *Science advances* **2020**, *6*, eabc8268.

(9) Arcari, M.; Söllner, I.; Javadi, A.; Lindskov Hansen, S.; Mahmoodian, S.; Liu, J.; Thyrrestrup, H.; Lee, E. H.; Song, J. D.; Stobbe, S.; others Near-unity coupling efficiency of a quantum emitter to a photonic crystal waveguide. *Physical review letters* **2014**, *113*, 093603.

(10) Liu, F.; Brash, A. J.; O'Hara, J.; Martins, L. M.; Phillips, C. L.; Coles, R. J.; Royall, B.; Clarke, E.; Bentham, C.; Prtljaga, N.; others High Purcell factor generation of indistinguishable on-chip single photons. *Nature nanotechnology* **2018**, *13*, 835–840.

(11) Da Lio, B.; Faurby, C.; Zhou, X.; Chan, M. L.; Uppu, R.; Thyrrestrup, H.; Scholz, S.; Wieck, A. D.; Ludwig, A.; Lodahl, P.; others A pure and indistinguishable single-photon source at telecommunication wavelength. *Advanced Quantum Technologies* **2022**, *5*, 2200006.

(12) Lee, J. Y.; Miroshnichenko, A. E.; Lee, R.-K. Simultaneously nearly zero forward and nearly zero backward scattering objects. *Optics Express* **2018**, *26*, 30393.

(13) Liu, W.; Kivshar, Y. S. Generalized Kerker effects in nanophotonics and meta-optics [Invited]. *Optics Express* **2018**, *26*, 13085.

(14) Bukharin, M. M.; Pecherkin, V. Y.; Ospanova, A. K.; Il'in, V. B.; Vasilyak, L. M.; Basharin, A. A.; Luk'yanchuk, B. Transverse Kerker effect in all-dielectric spheroidal particles. *Scientific Reports* **2022**, *12*.

(15) Khokhar, M.; Inam, F. A.; Nair, R. V. Kerker Condition for Enhancing Emission Rate and Directivity of Single Emitter Coupled to Dielectric Metasurfaces. *Advanced Optical Materials* **2022**, *10*.

(16) Person, S.; Jain, M.; Lapin, Z.; Sáenz, J. J.; Wicks, G.; Novotny, L. Demonstration of zero optical backscattering from single nanoparticles. *Nano letters* **2013**, *13*, 1806–1809.

(17) Li, R.; Zhou, X.; Panmai, M.; Xiang, J.; Liu, H.; Ouyang, M.; Fan, H.; Dai, Q.; Wei, Z. Broadband zero backward scattering by all-dielectric core-shell nanoparticles. *Optics Express* **2018**, *26*, 28891–28901.

(18) Fu, Y. H.; Kuznetsov, A. I.; Miroshnichenko, A. E.; Yu, Y. F.; Luk'yanchuk, B. Directional visible light scattering by silicon nanoparticles. *Nature communications* **2013**, *4*, 1527.

(19) Rocco, D.; Carletti, L.; Locatelli, A.; De Angelis, C. Controlling the directivity of all-dielectric nanoantennas excited by integrated quantum emitters. *Journal of the Optical Society of America B* **2017**, *34*, 1918.

(20) Di Francescantonio, A.; Zilli, A.; Rocco, D.; Coudrat, L.; Conti, F.; Biagioni, P.; Duò, L.; Lemaître, A.; De Angelis, C.; Leo, G.; others All-optical free-space routing of upconverted light by metasurfaces via nonlinear interferometry. *Nature Nanotechnology* **2024**, *19*, 298–305.

(21) Fagiani, L.; Bolzonello, L.; Osmond, J.; de Ceglia, D.; van Hulst, N.; Bollani, M.; Vincenti, M. A. Dual-Mode Polarization Control with Quasi-Bound States in the Continuum. *Advance Optical Material* **2018**, 2301456.

(22) Khorasaninejad, M.; Capasso, F. Metalenses: Versatile multifunctional photonic components. *Science* **2017**, *358*, eaam8100.

(23) Zotev, P. G.; Wang, Y.; Sortino, L.; Severs Millard, T.; Mullin, N.; Conteduca, D.; Shagar, M.; Genco, A.; Hobbs, J. K.; Krauss, T. F.; others Transition Metal Dichalcogenide Dimer Nanoantennas for Tailored Light–Matter Interactions. *ACS nano* **2022**, *16*, 6493–6505.

(24) Sortino, L.; Zotev, P.; Mignuzzi, S.; Cambiasso, J.; Schmidt, D.; Genco, A.; Aßmann, M.; Bayer, M.; Maier, S.; Sapienza, R.; others Enhanced light-matter interaction in an atomically thin semiconductor coupled with dielectric nano-antennas. *Nature communications* **2019**, *10*, 5119.

(25) Fagiani, L.; Gandolfi, M.; Carletti, L.; de Angelis, C.; Osmond, J.; Bollani, M. Modelling and nanofabrication of chiral dielectric metasurfaces. *Micro and Nano Engineering* **2023**, *19*, 100187.

(26) Solntsev, A. S.; Agarwal, G. S.; Kivshar, Y. S. Metasurfaces for quantum photonics. *Nature Photonics* **2021**, *15*, 327–336.

(27) Rutckaia, V.; Heyroth, F.; Novikov, A.; Shaleev, M.; Petrov, M.; Schilling, J. Quantum dot emission driven by Mie resonances in silicon nanostructures. *Nano letters* **2017**, *17*, 6886–6892.

(28) Bouchet, D.; Mivelle, M.; Proust, J.; Gallas, B.; Ozerov, I.; Garcia-Parajo, M. F.; Gulinatti, A.; Rech, I.; De Wilde, Y.; Bonod, N.; others Enhancement and inhibition of spontaneous photon emission by resonant silicon nanoantennas. *Physical Review Applied* **2016**, *6*, 064016.

(29) Staude, I.; Khardikov, V. V.; Fofang, N. T.; Liu, S.; Decker, M.; Neshev, D. N.; Luk, T. S.; Brener, I.; Kivshar, Y. S. Shaping photoluminescence spectra with magnetoelectric resonances in all-dielectric nanoparticles. *Acs Photonics* **2015**, *2*, 172–177.

(30) Sortino, L.; Zotev, P. G.; Phillips, C. L.; Brash, A. J.; Cambiasso, J.; Marensi, E.; Fox, A. M.; Maier, S. A.; Sapienza, R.; Tartakovskii, A. I. Bright single photon emitters

with enhanced quantum efficiency in a two-dimensional semiconductor coupled with dielectric nano-antennas. *Nature communications* **2021**, *12*, 6063.

(31) Rocco, D.; Locatelli, A.; Carletti, L.; Vincenti, M. A.; De Angelis, C. Nonlinear asymmetric imaging with AlGaAs metasurface. *Optics Express* **2024**, *32*, 11673–11680.

(32) Gurioli, M.; Wang, Z.; Rastelli, A.; Kuroda, T.; Sanguinetti, S. Droplet epitaxy of semiconductor nanostructures for quantum photonic devices. *Nature Materials* **2019**, *18*, 799.

(33) Watanabe, K.; Koguchi, N.; Gotoh, Y. Fabrication of GaAs Quantum Dots by Modified Droplet Epitaxy. *Jpn. J. Appl. Phys.* **2000**, *39*, L79.

(34) Tuktamyshev, A.; Fedorov, A.; Bietti, S.; Vichi, S.; Zeuner, K. D.; Jöns, K. D.; Chrastina, D.; Tsukamoto, S.; Zwiller, V.; Gurioli, M.; Sanguinetti, S. Telecom-wavelength InAs QDs with low fine structure splitting grown by droplet epitaxy on GaAs(111)A vicinal substrates. *Applied Physics Letters* **2021**, *118*, 133102.

(35) Basset, F. B.; Bietti, S.; Tuktamyshev, A.; Vichi, S.; Bonera, E.; Sanguinetti, S. Spectral broadening in self-assembled GaAs quantum dots with narrow size distribution. *Journal of Applied Physics* **2019**, *126*, 024301.

(36) Bietti, S.; Basset, F. B.; Tuktamyshev, A.; Bonera, E.; Fedorov, A.; Sanguinetti, S. High – temperature droplet epitaxy of symmetric GaAs / AlGaAs quantum dots. *Scientific Reports* **2020**, *10*, 6532.

(37) Sanguinetti, S.; Bietti, S.; Koguchi, N. *Droplet epitaxy of nanostructures*; Elsevier, 2018; pp 293–314.

(38) Horikoshi, Y.; Kawashima, M.; Yamaguchi, H. Migration-Enhanced Epitaxy of GaAs and AlGaAs. *Jpn. J. Appl. Phys.* **1988**, *27*, 169.

(39) Tognazzi, A.; Okhlopkov, K. I.; Zilli, A.; Rocco, D.; Fagiani, L.; Mafakheri, E.; Bollani, M.; Finazzi, M.; Celebrano, M.; Shcherbakov, M. R.; others Third-harmonic light polarization control in magnetically resonant silicon metasurfaces. *Optics Express* **2021**, *29*, 11605–11612.

(40) Tavani, G.; Chiappini, A.; Fedorov, A.; Scotognella, F.; Sanguinetti, S.; Chrastina, D.; Bollani, M. Tailoring of embedded dielectric alumina film in AlGaAs epilayer by selective thermal oxidation. *Optical Materials Express* **2022**, *12*, 835.

(41) Carletti, L.; Rocco, D.; Locatelli, A.; De Angelis, C.; Gili, V. F.; Ravaro, M.; Favero, I.; Leo, G.; Finazzi, M.; Ghirardini, L.; Celebrano, M.; Marino, G.; Zayats, A. V. Controlling second-harmonic generation at the nanoscale with monolithic AlGaAs-on-AlOx antennas. *Nanotechnology* **2017**, *28*, 114005.

(42) Genco, A.; Cruciano, C.; Corti, M.; McGhee, K. E.; Ardini, B.; Sortino, L.; Huttenhofer, L.; Virgili, T.; Lidzey, D. G.; Maier, S. A.; others k-Space hyperspectral imaging by a birefringent common-path interferometer. *ACS photonics* **2022**, *9*, 3563–3572.

TOC Graphic

Some journals require a graphical entry for the Table of Contents. This should be laid out "print ready" so that the sizing of the text is correct.
Inside the `tocentry` environment, the font used is Helvetica 8 pt, as required by *Journal of the American Chemical Society*.
The surrounding frame is 9 cm by 3.5 cm, which is the maximum permitted for *Journal of the American Chemical Society* graphical table of content entries. The box will not resize if the content is too big: instead it will overflow the edge of the box.
This box and the associated title will always be printed on a separate page at the end of the document.